Materials Research Express

PAPER • **OPEN ACCESS**

A systematic variation in cationic distribution and its influence on the magnetization of mixed-metal (nickel and zinc) cobaltite spinels

To cite this article: Wanchai Deeloed *et al* 2020 *Mater. Res. Express* **7** 096104

Materials Research Express

OPEN ACCESS

RECEIVED
8 August 2020

REVISED
26 August 2020

ACCEPTED FOR PUBLICATION
3 September 2020

PUBLISHED
23 September 2020

PAPER

A systematic variation in cationic distribution and its influence on the magnetization of mixed-metal (nickel and zinc) cobaltite spinels

Wanchai Deeloed[1,2], **Worawat Wattanathana**[3], **Pongsakorn Jantaratana**[4], **Panida Prompinit**[5], **Suttipong Wannapaiboon**[6], **Suparat Singkammo**[6], **Suchinda Sattayaporn**[6], **Apirat Laobuthee**[3], **Songwut Suramitr**[1,2,*] and **Yuranan Hanlumyuang**[3,*]

[1] Department of Chemistry, Faculty of Science, Kasetsart University, Bangkok 10900, Thailand
[2] Center for Advanced Studies in Nanotechnology for Chemical, Food and Agricultural Industries, KU Institute for Advanced Studies, Kasetsart University, Bangkok 10900, Thailand
[3] Department of Materials Engineering, Faculty of Engineering, Kasetsart University, Bangkok 10900, Thailand
[4] Department of Physics, Faculty of Science, Kasetsart University, Bangkok 10900, Thailand
[5] Hybrid Nanostructure and Nanocomposites Laboratory, National Nanotechnology Center (NANOTEC), National Science and Technology Development Agency (NSTDA), Pathum Thani 12120, Thailand
[6] Synchrotron Light Research Institute, 111 University Avenue, Suranaree, Muang, Nakhon Ratchasima 30000, Thailand
[*] Authors to whom any correspondence should be addressed.

E-mail: fsciswsm@ku.ac.th **and** yuranan.h@ku.th

Keywords: cobaltite spinel, x-ray techniques, cationic distribution, magnetization

Supplementary material for this article is available online

Abstract

Cobaltite oxide spinel ($CoCo_2O_4$) is one promising material that has been extensively studied for decades due to its versatile applications. Revealing the correlation among chemical compositions, cationic distributions, and physical properties are crucial for exploring its novel application. Here, a series of nickel/zinc co-substituted cobaltite spinels, $Zn_{1-X}Ni_XCo_2O_4$ (ZNCO-X; where X = 0.00, 0.25, …, 1.00), was synthesized by calcining the hydrothermal-derived precursors and their magnetic properties have been investigated. Multiple x-ray based characterization techniques (XRD, XRF, XPS, and XAS) were applied to determine the crystalline structure and appropriated compositions of cation species (Zn^{2+}, Ni^{2+}, Ni^{3+}, Co^{2+}, and Co^{3+}). In conjunction with Neel's theory of antiferromagnetism, the theoretical magnetization of the spinel series was calculated based on the assumption that Zn^{2+} ion was located in tetrahedral (A site) while nickel cations (Ni^{2+} and Ni^{3+}) occupying the octahedral (B site). The theoretical magnetization profile exhibited a good correlation. Superparamagnetic effect and cationic site exchange can be used to explain the discrepancies between the measured and calculated magnetizations. This work reported a systematic controlling of materials structure and cationic distribution, which are crucial for fine-tuning the magnetic property of the $Zn_{1-X}Ni_XCo_2O_4$ cobaltite system.

1. Introduction

Spinel oxides are known as one of the major types of ceramic oxides [1]. Classified in the space group of Fd $\bar{3}$ m, their crystalline framework has been considered as a cubic close packing array of oxide anions (O^{2-}) incorporating cationic occupancy sites. Generally, for the normal spinel, one-eighth of the tetrahedral sites (A site) is occupied by divalent cations, while one-half of the octahedral sites (B site) is filled by the trivalent cations. A general empirical formula, AB_2O_4 (where A and B determine the cations which occupied the A site and B site, respectively), has been introduced to represent this ceramic oxide [1, 2]. The inversion of the described cationic occupancy pattern results in an inverse spinel. Well-known spinel oxides include magnetite (Fe_3O_4), cuprospinel ($CuFe_2O_4$), and chromite ($FeCr_2O_4$), among others.

Cobaltite spinel, $CoCo_2O_4$ (or Co_3O_4), is another important binary metal oxide in this group, mainly due to its multivalent cobalt cations. $CoCo_2O_4$ provides applications in magnetic semiconductors [3] and

electrochemical catalysts as an electrode material [4, 5]. However, its performance is still below the satisfactory level due to its low electrical conductivity ranging from only 10^{-3} to 10^{-4} S · cm^{-1} [6]. Furthermore, cobalt is poisonous and expensive, leading to the incorporation of other first-row transition metals such as Mn, Fe, and Ni into the cobaltite spinel framework forming a family of ternary metal oxides [4–7]. Among them, nickel cobaltite spinel ($NiCo_2O_4$) has gained considerable attention due to its outstanding performance in redox-chemistry [8]. $NiCo_2O_4$ has been reported as an inverse-type spinel with the co-existence of multivalent cations, *i.e.*, Ni^{2+}, Ni^{3+}, Co^{2+}, and Co^{3+} in the structure [2, 4, 9, 10]. Recently, it has been recognized as an emerging material with potential applications in supercapacitors [9, 11, 12], lithium storage batteries [13], and fuel cells [8]. Its outstanding performance is attributed to its relatively high conductivity and high battery rate capability [14]. Another interesting member of the cobaltite group is $ZnCo_2O_4$. It has been known as a normal spinel, with high potential in photocatalysis applications [15, 16] and energy storage applications [17]. However, the catalytic activity of $ZnCo_2O_4$ was found to be lower than that of $NiCo_2O_4$, due to its lower conductivity [16]. The improved electrical property of $ZnCo_2O_4$ has been reported in previous studies [18–22].

In this work, we intended to synthesize a series of mixed-metal cobaltite oxide spinel, namely $Zn_{1-X}Ni_XCo_2O_4$ (where X = 0.00, 0.25, …, 1.00), to establish the correlation among chemical compositions, cationic distributions, and magnetic properties. With this respect, a series of cobaltite spinels with a desired fraction of nickel and zinc was synthesized using a hydrothermal-crystallization procedure, together with subsequent oxidative thermal decomposition reaction. Synchrotron-based techniques have been utilized to provide such comprehensive information about cationic species located within the structure. We found that the incorporation of different cationic species into the cobaltite spinel can cause a significant change in the cationic distribution, the valency states of cations which triggered a systematic change in the material magnetization.

2. Experimental

2.1. Synthesis of cobaltite spinel and derivatives

Analytical grade chemicals were used for material synthesis without further purification. In this present work, $CoCo_2O_4$ (hereafter denoted as CCO) was used as reference material to compare and examine the effects of nickel and zinc doping in various aspects. This reference spinel was derived from its precursor compound synthesized by the hydrothermal approach. To synthesize the CCO precursor, cobalt(II) acetate tetrahydrate ($Co(CH_3COO)_2 \cdot 4H_2O$), and urea ($NH_2CONH_2$) with the mole ratio of 3:3.33 were dissolved in DI water. The mixture was stirred to obtain a clear reddish solution. The solution was sealed in a 125 ml Teflon-liner stainless steel autoclave, keeping a constant fill factor of 50% by volume. The hydrothermal synthesis was carried out at 180 °C for 12 h to obtain the CCO precursor as a pink precipitate. Then, the CCO precursor was filtered out and subsequently washed with DI water and absolute ethanol. The CCO precursor was dried at 60 °C overnight and converted to the desired CCO spinel by calcination at 480 °C for 10 h. The calcined sample was stored in a desiccator and finely ball-milled before characterization.

In order to prepare a series of nickel/zinc co-substituted cobaltite derivatives, $Zn_{1-X}Ni_XCo_2O_4$ spinels (ZNCO-X, where X = 0.00, 0.25 0.50, 0.75, 1.00), the same synthesis protocol was applied, but one-third of the cobalt(II) acetate tetrahydrate content was replaced with the mixed substituents between zinc(II) acetate dihydrate ($Zn(CH_3COO)_2 \cdot 2H_2O$) and nickel(II) nitrate hexahydrate ($Ni(NO_3)_2 \cdot 6H_2O$). Throughout this work, the parameter X referred to the mole fraction of the nickel salt added in the precursor synthetic step. The mole ratio between the mixed substituents to the cobalt salt to the urea was kept as 1:2:3.33 in all cases. It should be noted that the exact molar ratio of each metal component within the obtained spinel products was characterized by synchrotron-based x-ray fluorescence spectroscopy.

2.2. Material characterization

2.2.1. Powdered x-ray diffraction (PXRD)

The crystal structure of the obtained samples was investigated using a PANalytical (AERIS) x-ray diffractometer in Bragg-Brentano geometry equipped with a Cu-K_α radiation source, Cu-K_β cut-off filtered, (λ = 1.544 Å, 15 mA, 45 kV, 600 W) and ultrafast solid-state PIXcel^{1D} detector. All samples were scanned in a continuous mode on a rotating stage at the 2θ range from 15° to 70° with a step resolution of 0.02°. Post-subtracted diffractogram was obtained by the X'Pert HighScore Plus program (version 2.1, PANalytical B.V. (2004)), together with the PDF2 PAN database. The Bragg's positions and the full-width at half maximums (FWHM) of each sample were determined by the software.

2.2.2. Electron microscope

Morphologies and surface topographies of the prepared spinel materials have been investigated by a Field-emission scanning electron microscope (FESEM, JEOL-JSM-7600F) using an operating voltage of 5 kV.

Furthermore, a field-emission transmission electron microscope (FETEM, JEOL-JEM-3100F at operating voltage 300 kV) was also employed to directly visualize the micro and nanostructures of the prepared materials.

2.2.3. Cationic composition determination

Herein, several synchrotron-based techniques at Synchrotron Light Research Institute (SLRI), Nakhon Ratchasima, Thailand, including x-ray absorption spectroscopy (XAS), x-ray photoelectron spectroscopy (XPS), and x-ray fluorescence spectroscopy (XRF), were integrated to determine the best representative cationic compositions of all prepared samples. Fine powders obtained by the ball-milling process were used for XAS, XPS, and XRF investigations. Firstly, we recorded XAS spectra (Co, Ni and Zn K-edges) in an x-ray absorption near edge structure (XANES) region at the SUT-NANOTEC-SLRI (Beamline 5.2) using Ge (220) as a double crystal monochromator (DCM). Energy calibration was carried out with standard metallic foils of cobalt, nickel and zinc [23]. All obtained XANES spectra were further normalized using Athena program (Demeter 0.9.26, Ifeffit 1.2.12) [24]. Secondly, the XRF experiment was performed at Beamline 1.1W (Multiple x-ray Techniques, MXT) using a 19-elements Ge detector as the detector. The samples were exposed to the monochromatic synchrotron x-ray radiation with the energy of 10 keV for 300 s. The obtained XRF data were further analyzed using the PyMCA software. Lastly, standalone XPS (PHI5000 VersaProbe II, ULVAC-PHI, Japan, Al Kα source) has been performed at the SUT-NANOTEC-SLRI joint research facility (BL5.3). The powder samples have sparsely adhered on the conductive carbon tape without surface modification. The samples were investigated in both wide scan (pass energy 1174 eV, energy step 1.0 eV) and high-resolution scan (pass energy 46.95 eV, energy step 0.05 eV) for C_{1s}, O_{1s}, Co_{2p}, Ni_{2p}, and Zn_{2p}. The XPS spectra were normalized and deconvoluted using the Multipak software (v9.0).

2.2.4. Vibrating sample magnetometer (VSM)

A vibrating sample magnetometer (VSM), custom made by the Department of Physics, Kasetsart University, Thailand, was utilized to evaluate the magnetic susceptibility (M_s) of the synthesized samples [25, 26]. Prior to the measurement, the sample powder was pre-shaped into a pellet via a mold-pressing method, using a uniaxial mold method (the applied pressure of 10 kPa) without any additive chemicals. The applied external magnetic field was within the range of $\pm$10.0 kOe at room temperature. The VSM system was calibrated with a 3 mm diameter Ni sphere (Lake Shore 730908). The magnetic moment measurement accuracy is better than 1.5% of reading.

3. Results and discussion

3.1. Materials structure, cationic composition, and observed magnetization

3.1.1. Powdered x-ray diffraction (PXRD)

The phase formations and crystal structures of the post-calcined samples were examined by XRD technique. As illustrated in figure 1(a), the post-calcined CCO sample showed a diffracted pattern that was identical to the cubic $CoCo_2O_4$ spinel, space group Fd $\bar{3}$m (PDF# 01-076-1802). The diffracted peaks positioned at 19.0°, 31.3°, 36.9°, 38.5°, 44.8°, 55.7°, 59.4°, and 65.2° were indexed to the Bragg's angles of reflections from the planes (111), (220), (311), (222), (400), (422), (511) and (440) of the $CoCo_2O_4$ spinel, respectively. The result confirmed the advantage of the synthesis approach in terms of providing such high purity of the targeted spinel oxide compound. Furthermore, from figure 1(a), the post-calcine samples containing different nickel and zinc substitution fraction (ZNCO-X where X = 0.00 to 1.00) also exhibited the diffracted patterns nearly identical to that of the parent CCO standard sample. Hence, the results confirmed that the cobaltite spinel framework was preserved across all samples.

Further analysis of PXRD data [27–29] indicated that the substitution by nickel and zinc provides an overall expansion of the unit cell with respect to the cobaltite spinel structure as evidenced by the increasing parameter (a) in the expression;

$$\frac{1}{d_{hkl}^2} = \frac{h^2 + k^2 + l^2}{a^2} \tag{1}$$

where d is the interplanar spacing, and h, k, l are the Miller indices. The estimated lattice parameter was tabulated in table 1 and plotted in figure 1(b). The ZNCO-0.00 sample had a lattice parameter *ca.* 8.092 $\pm$ 0.006 Å which is slightly larger than that of $CoCo_2O_4$ parent spinel (*ca.* 8.088 $\pm$ 0.003 Å). Moreover, by introducing more nickel content (from X = 0.25 to 1.00), the amount of elongation was progressively enhanced. The small change on spinel framework upon the varying nickel and zinc incorporation stems from the fact that cobalt, nickel and zinc are all adjacent first-row transition metal elements and their cationic radii are rather similar (Co^{2+} = 79 pm, Co^{3+} = 69 pm, Ni^{2+} = 69 pm, Ni^{3+} = 70 pm and Zn^{2+} = 74 pm) [1]. This has led to the successful

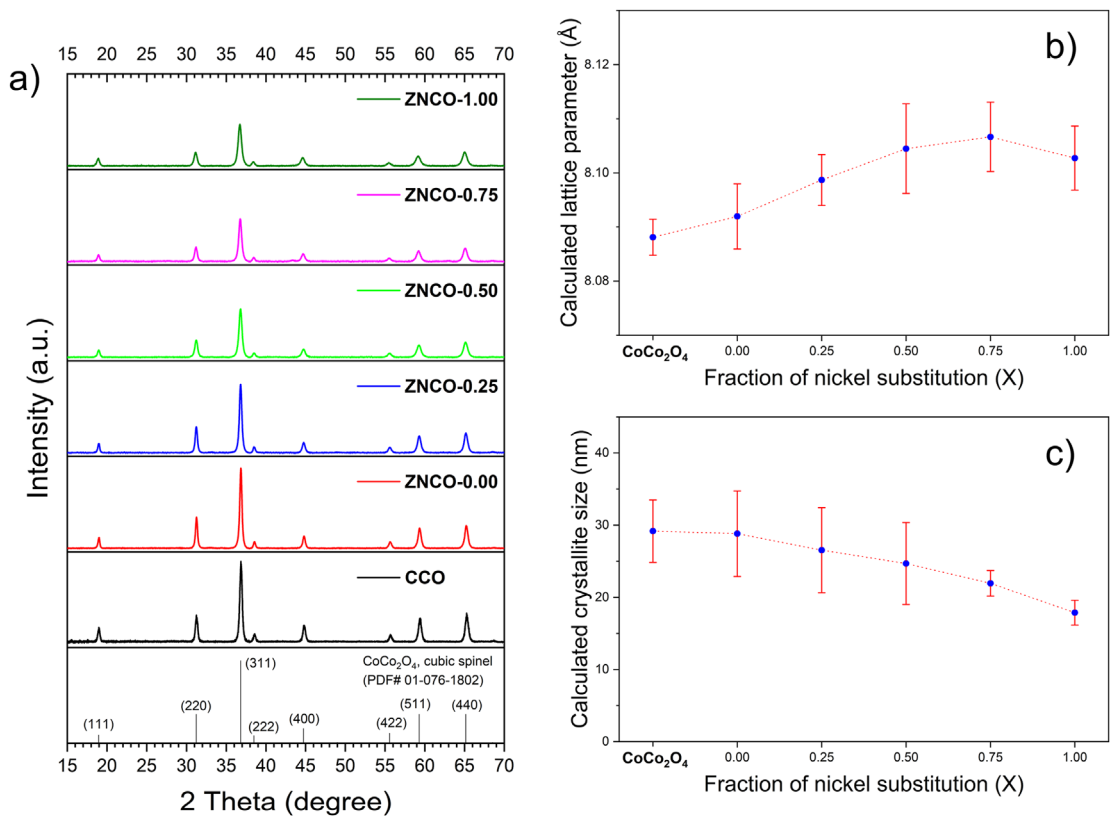

Figure 1. (a) X-ray diffractograms of the prepared spinel samples. Further analysis of the diffractogram data gave the profile of (b) calculated lattice parameter and (c) calculated crystalline grain size of the mixed-metal spinels.

Table 1. Summary of calculated crystallite sizes and lattice parameters of the synthesized spinels.

Spinel compounds	Calculated crystallite size (nm)	Calculated lattice parameter (Å)
ZNCO-1.00	17.88 ± 1.72	8.103 ± 0.006
ZNCO-0.75	21.96 ± 1.77	8.107 ± 0.006
ZNCO-0.50	24.69 ± 5.67	8.104 ± 0.008
ZNCO-0.25	26.53 ± 5.89	8.099 ± 0.005
ZNCO-0.00	28.82 ± 5.92	8.092 ± 0.006
$CoCo_2O_4$ (syn.)	29.17 ± 4.31	8.088 ± 0.003

incorporation of mixed metal ions in the form of a solid solution without the presence of additional crystalline phases.

Regarding the effects of the Zn and Ni-doping on the crystallite sizes, the crystallite size (D) of samples was calculated from the Scherrer equation;

$$D = \frac{0.9\lambda}{\beta \cos \theta} \tag{2}$$

where the x-ray wavelength (λ) is 1.5406 Å, θ is Bragg's angle of reflection, and the corrected peak at full width at half-maximum (FWHM) intensity is denoted by β. The crystallite sizes for the whole sample series were tabulated in table 1 and shown in figure 1(c). Crystallite size of the $CoCo_2O_4$ parent spinel and its zinc-substituted derivative (ZNCO-0.00) were comparable in sizes (*ca.* 29.17 ± 4.31 nm and 28.82 ± 5.92 nm), suggesting the slight effect of zinc content to the change in crystallite size. However, the nickel content in the mixed-metal spinel noticeably contributes to a reduction in the crystallite sizes; from *ca.* 26.53 ± 5.89 nm in ZNCO-0.25 to *ca.* 17.88 ± 1.72 nm in ZNCO-1.00). Nanosized cobaltite spinel particles were confirmed by SEM and TEM images, as reported in supporting information (figures S1 to S4 are available online at stacks.iop.org/MRX/7/096104/mmedia).

By closely inspecting the relative intensities of the (311) diffraction peak in figure 1(a), a different effect on the crystallinity of the prepared spinels with respect to the variation of nickel and zinc substitution contents was observed (see also table S1). For the samples with relatively high zinc substitution level, *i.e.*, ZNCO-0.00 (representing $ZnCo_2O_4$ spinel) and ZNCO-0.25, the degree of crystallinity was nearly the same as that of the CCO spinel. A good crystallinity on these samples might come from the fact that $ZnCo_2O_4$ and $CoCo_2O_4$ adapted a similar normal-type spinel structure. The Zn^{2+} dopants should substitute Co^{2+} ions in the tetrahedral sites (A site) [15]. On the other hand, the lower degree of crystallinity was clearly observed in the case of the relatively high nickel substituted samples, *i.e.*, ZNCO-0.75 and ZNCO-1.00 (representing $NiCo_2O_4$ spinel). According to literature, $NiCo_2O_4$ has been recognized as an inverse-type spinel compound, in which octahedral sites (B site) are half-filled by Ni^{2+} and Co^{3+} cations, while another half of the Co^{3+} ions occupied the tetrahedral (A site) instead. Thus, the accommodation of the nickel inside the cobaltite spinel compound would be anticipated to cause some extent of configurative rearrangement of the occupancy and the overall crystal framework. This site exchange is believed to be the origin of the lower degree of crystallinity. Consequently, the observed XRD peak intensities at the (311) plane were significantly reduced with respect to the elevating nickel content.

Modern science and technology allow for an accurate non-destructive determination of chemical composition by using some specialized x-ray spectroscopy techniques. In the forthcoming sections, the analysis of the XRF, XPS, and XAS techniques will be discussed in detail. In order to avoid the lengthy discussion across all sample types, the experimental data and analysis would be significantly devised for the particular sample of ZNCO-0.50. The spinel ZNCO-0.50 sample will be used as a representative sample for the main discussion. Essential results for all samples have been individually reported in the supporting information (tables S2 to S9).

3.1.2. X-ray fluorescence spectroscopy (XRF)

X-ray fluorescence (XRF) technique has been carried out to provide insights into the elemental compositions of each post-calcined sample. As shown in figure 2, the characteristic fluorescence signals, including K_α and K_β of cobalt, nickel and zinc inside the ZNCO-0.50 sample, were clearly indexed. Moreover, the XRF spectra of other samples can be found in figure S5. Those prominent emission bands have been deconvoluted and re-assigned according to their characteristic energy, as indicated in figure 2. The integrated peak areas of each metal element were also derived from the spectra and used to calculate the ratio of each metal element within the spinel samples according to the details in the following paragraph.

Suppose that all metal elements were confined within the spinel framework, the whole integrated metal peak area would be scaled to the value of 3.00, which is the number of the total cationic species in spinel (AB_2O_4). Therefore, the content of the metal element of interest in the spinel was represented by an area percentage of the all-metal peak areas (as shown in the inset of figure 2). Using such an assumption, the exact formula of the post-calcined ZNCO-0.5 sample can be written as $Zn_{0.58}Ni_{0.40}Co_{2.02}O_4$. This same protocol was applied throughout the sample series to determine the chemical compositions of all spinel samples (summarized in table S2). According to the information in table S2, the existing nickel content in all nickel-contained spinels seems significantly lower than our anticipation. The vanished nickel content, *ca.* 25% from the desired fraction referring to the initial molar ratio at the precursor synthetic step, was mostly compensated by the presence of zinc. This was because zinc cation might crystallize more rapidly than nickel cation under the studied hydrothermal conditions.

3.1.3. X-ray photoemission spectroscopy(XPS)

After a successful determination of the chemical formulae, more detail on the metal valency state was further investigated by x-ray photoelectron spectroscopy (XPS). Figure 3(a) shows wide scan spectra of the post-calcined ZNCO-0.50 sample, revealing the existence of O_{1s}, Co_{2p}, $Ni_{2p,}$ and Zn_{2p} as indicated. XPS spectra of other samples are displayed in figure S6. Deconvolution of the O_{1s} high-resolution spectra (figure 3(b)) determined two distinct types of oxygenated species, assigned as the oxygen anion bound to metal cation (528.8 eV) and the chemisorbed oxygen species (531.4 eV), respectively. Importantly, there is no sign of oxygen vacancy found in the O_{1s} spectra, implying the reliability of oxygen stoichiometry in the previously proposed formulae of ZNCO-0.50 sample. The XPS high-resolution spectra of transition metals (figures 3(c) to (e)) showed the spin-orbit doublet, indicating the d-orbital ligand field splitting ($M_{2p3/2}$ and $M_{2p1/2}$; M = Co, Ni, and Zn) caused by the surrounding oxygen anion. Deconvolution of the $Co_{2p3/2}$ confirmed the co-existence of Co^{3+} (779.9 eV) and Co^{2+} (781.3 eV) inside the sample (figure 3(c)), incorporated with the broad shake-up satellite peak at 784.0 eV. For $Ni_{2p3/2}$ (figure 3(d)), the presence of both Ni^{2+} and Ni^{3+} was confirmed by the deconvoluted peaks at 854.1 and 855.9 eV, and followed by the shake-up satellite peak at 861.2 eV. For $Zn_{2p3/2}$, the existence of Zn^{2+} ion was found as the prominent emission at 1021.2 eV (figure 3(e)). Therefore, XPS results confirm the existence of multivalence cation species, *i.e.*, Co^{2+}, Co^{3+}, Ni^{2+}, Ni^{3+} and Zn^{2+}, inside the prepared ZNCO-0.50 spinel sample.

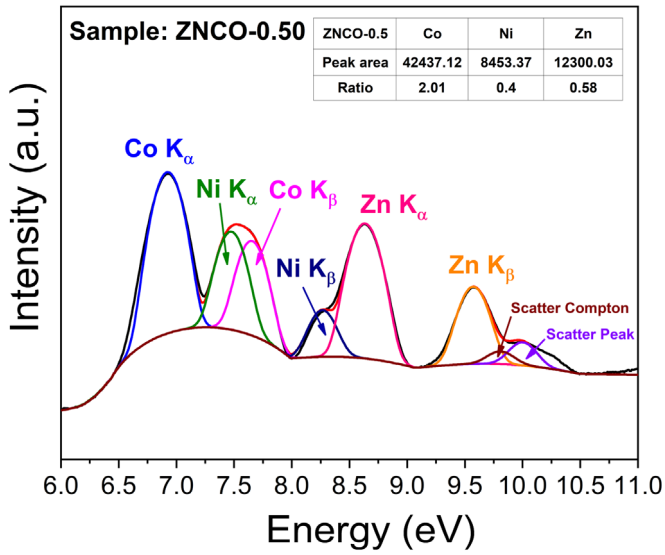

Figure 2. X-ray fluorescence (XRF) spectra (obtained by using the monochromatic synchrotron-based x-ray excitation with an energy of 10 keV) of the post calcined ZNCO-0.50 spinel sample.

Furthermore, the sensitivity of XPS was high enough to observe the variance in the relative amount of multivalence cations (Ni^{2+} and Ni^{3+}) as a function of the substitution factor (X) in the precursor. By investigating the relative peak area, between Ni^{2+} and Ni^{3+} species throughout the sample series, a systematic change of their percentage contribution was revealed (see table S3). It was found that at the early stage of nickel introduction ($X = 0.25$), the Ni^{3+} was rather a dominant species, *ca.* 80% than the Ni^{2+} ion. The contribution of Ni^{3+} was decreased upon an elevating nickel content, to be *ca.* 70%. In contrast to the case of cobalt, the XPS study indicated a stable Co^{2+} to Co^{3+} ratio, which fluctuated near a ratio of 50:50 in most of the samples (see table S3). Despite a perfect theoretical value for pristine cobaltite spinel ($CoCo_2O_4$), 33% of Co^{2+}, and 67% of Co^{3+}, that observed ratio by XPS seems to be far misplaced. This error might come from the fact that XPS is a surface-sensitive technique which cannot bring out the signals from the bulk matrix. Hence, we avoid calculating cationic compositions based on XPS results. However, without the loss in generality, the XPS spectra could still confirm the presence of cationic species inside the post-calcined products, namely Co^{2+}, Co^{3+}, Ni^{2+}, Ni^{3+} and Zn^{2+}.

3.1.4. X-ray absorption spectroscopy (XAS)

X-ray absorption spectroscopy (XAS) has been performed to quantify a certain level of cationic species. Figures 4(a) to (c) show the K-edges XANES spectra of cobalt, nickel, and zinc in the ZNCO-0.50 spinel sample, respectively. XAS spectra of all synthesized samples are shown in figure S7. Considering the XANES spectra probed at zinc K-edge (figure 4(c)), the absorption edge of zinc species presented in the synthesized spinel compound was lied within the edge of Zn^{2+} standard compounds, ZnO and $Zn(NO_3)_2$. Therefore, the result suggested the divalent state of zinc cation inside the ZNCO-0.50 spinel as expected.

The determination of the valency state of nickel was more complicated than zinc since the compound contained multivalence states of nickel ions, as previously confirmed by XPS. We found it was more convenient to determine the average valency state of nickel ions using XANES data. The average valency state was determined by the method used for $NiCo_2O_4$ compound as reported in the literature [27–29]. In a typical procedure, the photon energy at 0.5 normalized absorptions of the Ni K-edge spectra was selected as the representative energy for edge position, and compared with the position of the NiO standard compound to determine edge shift in eV [27, 28, 30]. Referring to the linear relationship of energy shift (+1.5 eV per +1 oxidation state) found by Mansour *et al* [27], the average oxidation state of nickel in our spinel can then be calculated. Note that the approximation method has been believed to contain 10% of uncertainty and more additional 5% of uncertainty from the monochromator [29]. Therefore, the estimated valency state will be rather reported as a value in one decimal place (see table S4). By using a simple mathematical conversion (see supporting information), the contribution of Ni^{2+} (6%) and Ni^{3+} (94%) in ZNCO-0.50 sample was obtained. Cation contribution for each sample has been reported in tables S5 to S9.

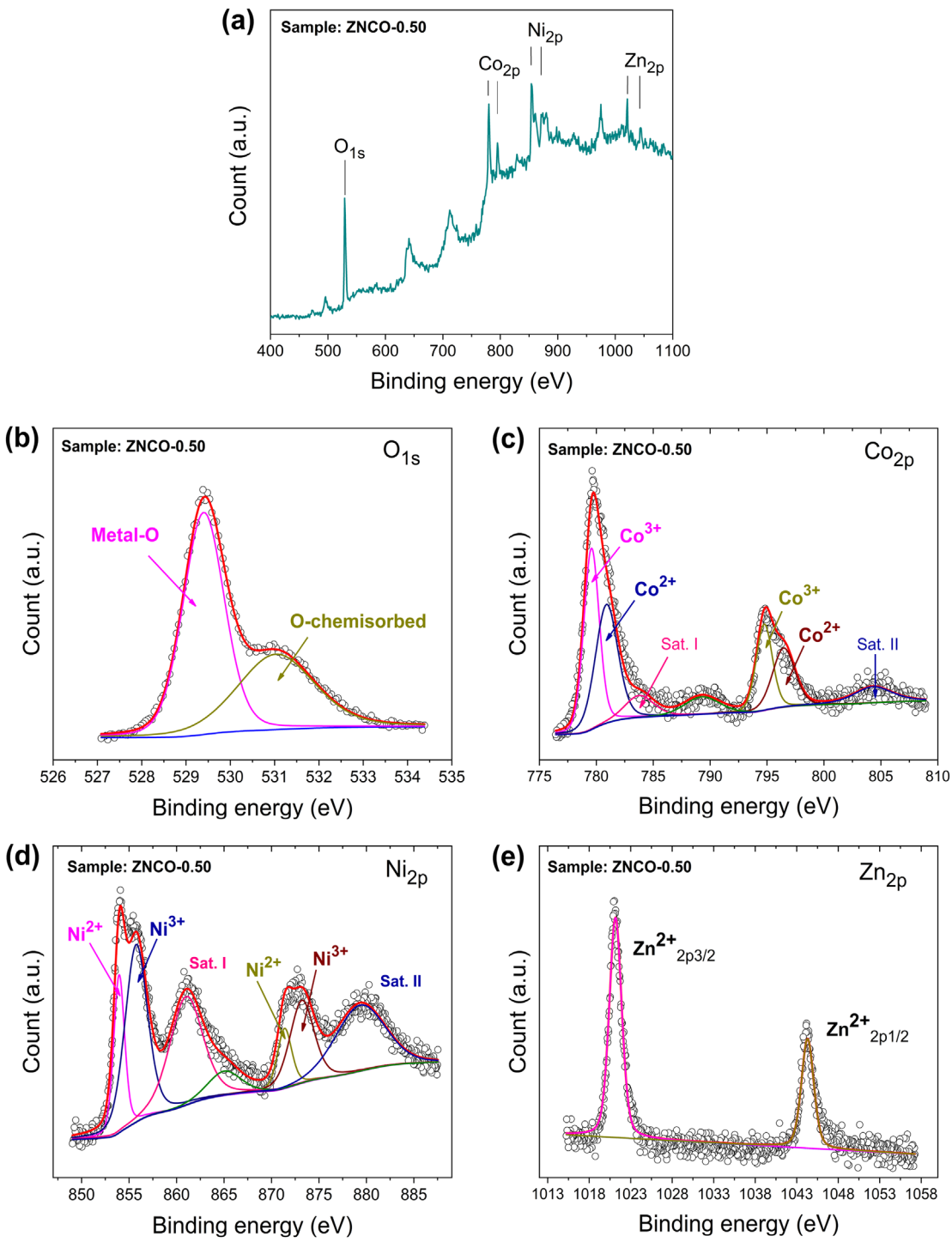

Figure 3. X-ray photoelectron spectra (XPS) of the post calcined ZNCO-0.50 spinel sample. The sample was investigated in (a) a wide scan and in a high-resolution scan for (b) O_{1s}, (c) Co_{2p}, (d) Ni_{2p} and (e) Zn_{2p}, respectively.

3.1.5. Vibrating sample magnetometer (VSM)

The effect of different nickel and zinc substitution fraction has been expressed through a variation of material magnetization. Magnetic properties at room temperature of all synthesized spinel samples were evaluated by a vibrating sample magnetometer (VSM). Experimental magnetization data was transformed from a measured value in emu $\cdot$ g^{-1} to the magnetic moment per formula unit ($n_B^{\exp}$) in $\mu_B \cdot$ f.u.$^{-1}$ through the following equation [31–33]; $n_B^{\exp} = (M_{fw} \times M_s^{\exp})/5585$, where $M_s^{\exp}$ was the magnetization in the unit of emu $\cdot$ g^{-1}, and M_{fw} was the spinel formula weight. As shown in figure 5(a), the VSM plot suggested a paramagnetic behavior in all synthesized spinel [1]. A sample with a higher X value exhibited a better sigmoidal curve without the magnetic hysteresis loop. A magnetic moment at $\pm$10 kOe of all prepared spinel did not reach the saturation

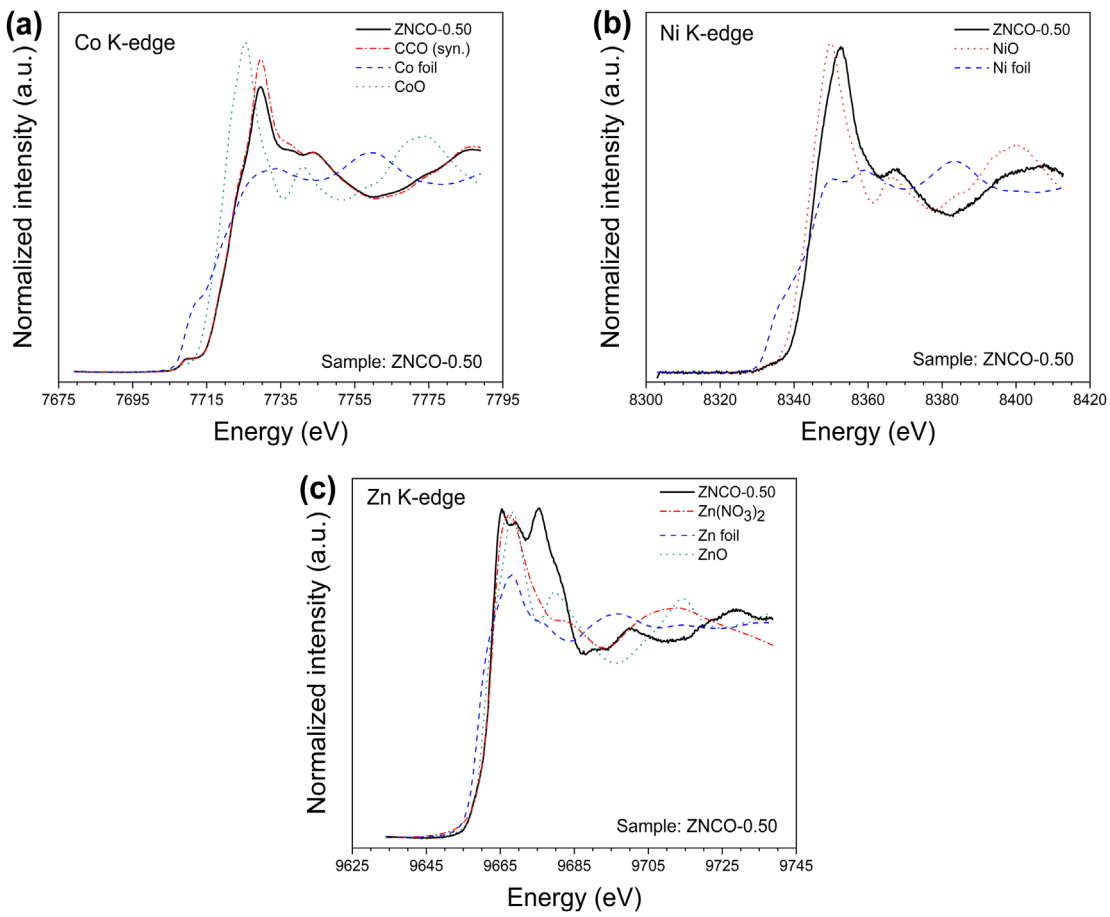

Figure 4. X-ray absorption near edge structure (XANES) spectra of the ZNCO-0.50 spinel sample. The sample was investigated at the K-edge of (a) cobalt, (b) nickel and (c) zinc. XANES spectra of some standard compounds were also demonstrated to compare the edge shift.

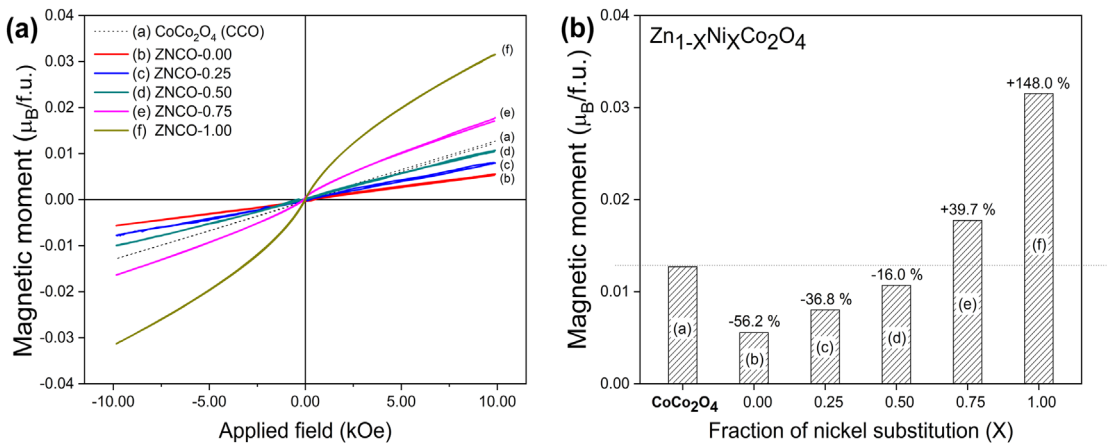

Figure 5. (a) Experimental magnetic moment per formula unit (in μ_B/f.u.) of all synthesized spinel samples. (b) a profile of magnetic moment change plotted as a function of the doping nickel fraction.

levels. As clearly seen in figure 5(a), the magnetic moments of the co-substituted samples were different from that of the parent CCO sample.

To better visualize the influence of the substitution fraction to the magnetization, the profiles of magnetic moments at +10 kOe as a function of the varying nickel substitution composition are depicted in figure 5(b). It was found that the magnetic moment of samples containing the highest zinc content, (ZNCO-0.00 or $ZnCo_2O_4$), was decreased 56% from that of the CCO spinel. In contrast, a recovery trend of the magnetization value has been observed by introducing the more nickel and the less zinc substituting content. In a sample that

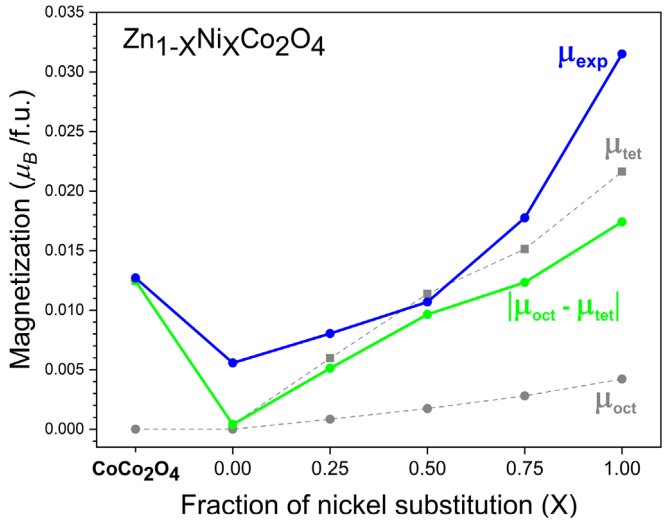

Figure 6. A profile comparison of (a) theoretical magnetizations obtained by Neel's theory and (b) experimental magnetizations measured by room temperature VSM. Theoretical magnetizations in both A and B sublattices was also plotted.

contained the highest amount of nickel introduction (ZNCO-1.00 or $NiCo_2O_4$), *ca.* 2.5 times the magnetic moment of the CCO parent was observed. The result shows that this magnetic moment profile would be correlated to the gradual normal-to-inverse transformation from the most normal-type spinel ($ZnCo_2O_4$) toward the most inverse-type spinel ($NiCo_2O_4$) in the mixed-metal series.

According to the numerous works regarding the magnetic properties of spinel-based materials, Neel's theory of antiferromagnetism has been widely cited for a useful explanation on the magnetic properties [31, 34, 35]. This theory has been applied for describing magnetic moments in materials containing two different sub-lattices (A and B sites) that aligned collinearly and anti-parallelly to each other due to the super-exchange interaction [1, 34]. To calculate a theoretical magnetic moment of an individual sample, the cationic distribution data would be essential. In the $CoCo_2O_4$ and $ZnCo_2O_4$ samples, the structure was known as normal spinel, while the $NiCo_2O_4$ sample adopts an inverse spinel structure. Therefore, the cationic distributions were assumed according to this information. All Zn^{2+} ions were assigned in the low-spin tetragonal site (A site) and all the nickel ions (both Ni^{2+} and Ni^{3+}) were assigned in the high-spin octahedral site (B site). The theoretical magnetization profiles for the synthesized spinel samples are displayed in figure 6. A correlation between the theoretical ($|\mu_{oct} - \mu_{tet}|$) and experimental magnetization values (μ_{exp}) for the whole series of the samples has been observed. The magnetic readings of the VSM system were calibrated so that the measurement accuracy is better than 1.5% of reading; hence no error bars were observed. The theoretical magnetizations exhibit the same tendency as the experimental values. However, the theoretical values were generally lower than the experimental ones.

The discrepancy might be, in part, explained by (i) the underestimation of the theoretical magnetization of ZNCO-0.75 and ZNCO-1.00 and (ii) the small-crystalline-size effect. The restricted distribution of Zn^{2+} over A site and Ni^{2+} and Ni^{3+} over B site lead to the underestimation of the theoretical magnetic moment due to some degree of site exchange between those cations. Such cationic redistribution led to the alteration of the total magnetization. In other material systems, Rietveld refinement and Bertaut method [36] are commonly used to determine cationic distribution in inorganic compounds. Both techniques rely on the x-ray diffraction signals that originated from the scattering of individual atoms in crystallographic planes. Unfortunately, the distinction of the isoelectronic cations (Ni^{3+} and Co^{2+}) like the present problem is a daunting task and requires complicated statistical analysis. The structural refinement to determine the cationic distribution in the ZNCO system was not pursued in this work. Note that neutron diffraction may provide better clarification of the existing cationic distribution within these obtained materials. However, the accessibility to the neutron diffraction facilities is rather limited in our cases. The detailed investigation of cationic distribution should be an interesting point for the further extension of this work.

Another possible explanation for discrepancies between the theoretical and the experimental magnetization values should be the effect of crystallite size. It has been reported that a paramagnetic substance with a few tenth-nanometer range of crystallite size can exhibit 'superparamagnetic' behavior. Evidently, from the XRD results, the spinel samples with smaller crystallite sizes were obtained when a higher nickel amount as seen from the Scherrer equation (figure 1(c)). Physical visualization using electron microscopes (both SEM and TEM) also confirmed that the employed synthesis route led to the nanosized crystallites. Most of the discrete paramagnetic

domains in the powder sample were presumably aligned by the applied external magnetic field [37, 38]. This external nanosized effect provides a surplus magnetic susceptibility to paramagnetic nanoparticles. Sigmoidal curve without the magnetic hysteresis loop on the ZNCO-1.00 sample (figure 5(a)) confirmed an establishment of a superparamagnetic effect on that sample [36–39].

By taking consideration of the XPS, XAS, and VSM results, we found a correlation between the amount of Ni^{2+} content and the resulting magnetization value. As the Ni^{2+} ions were increased, the magnetization value was highly increased because Ni^{2+} is a d^8 species that possessing the highest Bohr's magnetron (low spin O_h: t_{2g}^6, e_g^2; $\mu_B = 2$). On the contrary, Zn^{2+} is diamagnetic cation owing to its d^{10} electron (high spin T_d: e^4, t_2^6; $\mu_B = 0$). As a consequence, the sample with a higher nickel substitution fraction would reasonably have a higher magnetization value. Therefore, this work reported the systematic change in the magnetization of the ZNCO materials by adjusting the corresponding Zn^{2+} and Ni^{2+} contents.

4. Conclusions

In this work, we demonstrated the correlation among chemical compositions, cationic distributions, and magnetic properties of $Zn_{1-X}Ni_XCo_2O_4$ spinel (ZNCO-X; where X = 0.00, 0.25, 0.50, 0.75, 1.00). A series of cobaltite spinels was derived from its hydrothermally pre-formed precursors by thermal oxidation at 480 °C in atmospheric pressure. Herein, an integration of multiple characterization techniques relying on x-ray radiation (XRD, XRF, XPS, and XAS) was utilized. XRD technique confirmed that all resulting products were a pure crystalline phase of the cobaltite spinel. Analysis by XPS unveiled the presence of multivalent cationic species, *i.e.*, Co^{2+}, Co^{3+}, Ni^{2+}, Ni^{3+}, and Zn^{2+}. A combination of XRF and XAS provides a clue on the cationic composition. The distribution of cationic species over the spinel tetrahedral (A) and octahedral (B) sites has been assumed in order to calculate theoretical magnetization value regarding Neel's theory of antiferromagnetism. Interestingly, the variation of calculated magnetizations showed a similar trend with the experimental results. Deviations from the experimental values can be explained by a cationic site exchange and the superparamagnetic effect of the small-size particles. This study offers an insight into nickel and zinc ions in the mixed-metal cobaltite affects the structural switching between normal and inverse spinel, and hence their influence on the overall magnetic properties.

Acknowledgments

W D acknowledges the support from the Development and Promotion of Science and Technology Talents Project (DPST) scholarship. Y H would like to thank the Thailand Research Fund (TRF) and Kasetsart University for their joint support through the grant number TRG5880264 and the Kasetsart University Research and Development Institute (KURDI), Kasetsart University, Bangkok, Thailand. W D and S S would also acknowledge the Center for Advanced Studies in Nanotechnology for Chemical, Food and Agricultural Industries, KU Institute for Advanced Studies, Kasetsart University for the support. We are thankful to the Center of Nanotechnology, Department of Chemistry, Kasetsart University, the Department of Physics, Kasetsart University, and the Department of Materials Engineering, Kasetsart University, for the research facilities. We acknowledge the Synchrotron Light Research Institute (Public Organization), SLRI, Thailand for the provision of beamtime. All research staffs of BL1.1W (Multiple x-ray Techniques, MXT) and BL5.2 (SUT-NANOTEC-SLRI) at SLRI, are acknowledged for experimental consulting and assistance. Moreover, we would like to acknowledge Dr.Narong Chanlek from BL5.3 (SUT-NANOTEC-SLRI) for the informative XPS data acquisition and a conclusive interpretation.

Conflicts of interest

There are no conflicts to declare.

ORCID iDs

Wanchai Deeloed https://orcid.org/0000-0002-6706-6421
Worawat Wattanathana https://orcid.org/0000-0002-3592-3708
Pongsakorn Jantaratana https://orcid.org/0000-0002-4050-3628
Panida Prompinit https://orcid.org/0000-0001-6532-0724
Suttipong Wannapaiboon https://orcid.org/0000-0002-6765-9809
Suchinda Sattayaporn https://orcid.org/0000-0002-7618-8340

Apirat Laobuthee https://orcid.org/0000-0001-9744-9864
Songwut Suramitr https://orcid.org/0000-0002-6941-8814
Yuranan Hanlumyuang https://orcid.org/0000-0003-0252-1435

References

[1] Smart L E and Moore E A 1995 *Solid State Chemistry: an Introduction.* 2nd edition (London: Chapman & Hall)
[2] Wang R and Wu J 2017 5—structure and basic properties of ternary metal oxides and their prospects for application in supercapacitors *Metal Oxides in Supercapacitors* ed D P Dubal and P Gomez-Romero (Amsterdam: Elsevier) pp 99–132
[3] Chen J, Wu X and Selloni A 2011 Electronic structure and bonding properties of cobalt oxide in the spinel structure *Phys. Rev.* B **83** 245204
[4] Chang S-K *et al* 2015 Recent development in spinel cobaltites for supercapacitor application *Ceram. Int.* **41** 1–14
[5] Tan Y *et al* 2014 Insight the effect of surface Co cations on the electrocatalytic oxygen evolution properties of cobaltite spinels *Electrochim. Acta* **121** 183–7
[6] Shinde V R *et al* 2006 Supercapacitive cobalt oxide (Co_3O_4) thin films by spray pyrolysis *Appl. Surf. Sci.* **252** 7487–92
[7] Zhu J and Gao Q 2009 Mesoporous MCo_2O_4 (M = Cu, Mn and Ni) spinels: structural replication, characterization and catalytic application in CO oxidation. *Microporous Mesoporous Mater.* **124** 144–52
[8] Toh R J *et al* 2015 Ternary transition metal oxide nanoparticles with spinel structure for the oxygen reduction reaction *Chem. Electro. Chem.* **2** 982–7
[9] Dubal D P *et al* 2015 Nickel cobaltite as an emerging material for supercapacitors: an overview *Nano Energy* **11** 377–99
[10] Marco J F *et al* 2000 Characterization of the nickel cobaltite, $NiCo_2O_4$, prepared by several methods: an XRD, XANES, EXAFS, and XPS study *J. Solid State Chem.* **153** 74–81
[11] Guan B *et al* 2016 Morphology dependent supercapacitance of nanostructured $NiCo_2O_4$ on graphitic carbon nitride *Electrochim. Acta* **200** 239–46
[12] Wu Z, Zhu Y and Ji X 2014 $NiCo_2O_4$-based materials for electrochemical supercapacitors *J. Mater. Chem.* A **2** 14759–72
[13] Wang Y *et al* 2018 Facile preparation of monodisperse $NiCo_2O_4$ porous microcubes as a high capacity anode material for lithium ion batteries *Inorganic Chemistry Frontiers* **5** 559–67
[14] Wei T-Y *et al* 2010 A cost-effective supercapacitor material of ultrahigh specific capacitances: spinel nickel cobaltite aerogels from an epoxide-driven sol–gel process *Adv. Mater.* **22** 347–51
[15] Guo H *et al* 2014 Facile template-free one-pot fabrication of $ZnCo_2O_4$ microspheres with enhanced photocatalytic activities under visible-light illumination *Chem. Eng. J.* **239** 192–9
[16] Ndione P F *et al* 2014 Control of the electrical properties in spinel oxides by manipulating the cation disorder *Adv. Funct. Mater.* **24** 610–8
[17] Jiang F *et al* 2015 $ZnCo_2O_4$ nanoparticles/N-doped three-dimensional graphene composite with enhanced lithium-storage performance *Mater. Lett.* **161** 297–300
[18] Che H *et al* 2015 Three-dimensional hierarchical $ZnCo_2O_4$ flower-like microspheres assembled from porous nanosheets: Hydrothermal synthesis and electrochemical properties *Ceram. Int.* **41** 7556–64
[19] Bai J *et al* 2014 Unusual formation of $ZnCo_2O_4$ 3D hierarchical twin microspheres as a high-rate and ultralong-life lithium-ion battery anode material *Adv. Funct. Mater.* **24** 3012–20
[20] Mohamed S G *et al* 2013 Flower-like $ZnCo_2O_4$ nanowires: toward a high-performance anode material for Li-ion batteries *RSC Adv.* **3** 20143–9
[21] Paudel T R *et al* 2011 Asymmetric cation nonstoichiometry in spinels: site occupancy in Co_2ZnO_4 and Rh_2ZnO_4 *Phys. Rev.* B **84** 064109
[22] Paudel T R *et al* 2011 Doping rules and doping prototypes in A_2BO_4 spinel oxides *Adv. Funct. Mater.* **21** 4493–501
[23] Kidkhunthod P 2017 Structural studies of advanced functional materials by synchrotron-based x-ray absorption spectroscopy: BL5. 2 at SLRI, Thailand *Adv. Nat. Sci.: Nanosci. Nanotechnol.* **8** 035007
[24] Ravel B and Newville M 2005 ATHENA, ARTEMIS, HEPHAESTUS: data analysis for x-ray absorption spectroscopy using IFEFFIT *J. Synchrotron Radiat.* **12** 537–41
[25] Veranitisagul C *et al* 2016 $BaFe_{12}O_{19}$ from thermal decomposition of bimetallic triethanolamine complex as magnetic filler for bioplastics *Mater. Chem. Phys.* **177** 48–55
[26] Wattanathana W *et al* 2018 Barium ferrite prepared by modified Pechini method: effects of chloride and nitrate counter ions on microstructures and magnetic properties *J. Mater. Sci.: Mater. Electron.* **29** 1542–53
[27] Mansour A and Melendres C 1998 Analysis of x-ray absorption spectra of some nickel oxycompounds using theoretical standards *J. Phys. Chem.* A **102** 65–81
[28] Marco J F *et al* 2001 Cation distribution and magnetic structure of the ferrimagnetic spinel $NiCo_2O_4$ *J. Mater. Chem.* **11** 3087–93
[29] Loche D *et al* 2017 Cation distribution and vacancies in nickel cobaltite *Phys. Chem. Chem. Phys.* **19** 16775–84
[30] Grunes L 1983 Study of the K edges of 3 d transition metals in pure and oxide form by x-ray-absorption spectroscopy *Phys. Rev.* B **27** 2111
[31] Kavas H *et al* 2009 Cation distribution and magnetic properties of Zn doped $NiFe_2O_4$ nanoparticles synthesized by PEG-assisted hydrothermal route *J. Alloys Compd.* **479** 49–55
[32] Thanh N K *et al* 2016 Cation distribution in $CuFe_2O_4$ nanoparticles: effects of Ni doping on magnetic properties *J. Appl. Phys.* **120** 142115
[33] Nikam D S *et al* 2015 Cation distribution, structural, morphological and magnetic properties of $Co_{1-x}Zn_xFe_2O_4$ (x = 0–1) nanoparticles *RSC Adv.* **5** 2338–45
[34] Smart J S 1955 The néel theory of ferrimagnetism *Am. J. Phys.* **23** 356–70
[35] Battle P D, Cheetham A K and Goodenough J B 1979 A neutron diffraction study of the ferrimagnetic spinel $NiCo_2O_4$ *Mater. Res. Bull.* **14** 1013–24
[36] Najmoddin N *et al* 2014 XRD cation distribution and magnetic properties of mesoporous Zn-substituted $CuFe_2O_4$ *Ceram. Int.* **40** 3619–25
[37] Pankhurst Q A *et al* 2003 Applications of magnetic nanoparticles in biomedicine *J. Phys. D: Appl. Phys.* **36** R167–81
[38] Richardson J *et al* 1991 Origin of superparamagnetism in nickel oxide *J. Appl. Phys.* **70** 6977–82
[39] Papaefthymiou G C 2009 Nanoparticle magnetism *Nano Today* **4** 438–47